Wind and Structures, *Vol. 22, No. 4 (2016) 477-501*
DOI: http://dx.doi.org/10.12989/was.2016.22.4.477

Wind direction field under the influence of topography: part II: CFD investigations

S.W. Li*[1], Z.Z. Hu[1,2], K.T. Tse[3] and A.U. Weerasuriya[3]

[1]*Division of Ocean Science and Technology, Graduate School at Shenzhen, Tsinghua University, Shenzhen, P.R. China*
[2]*Department of Civil Engineering, Tsinghua University, Beijing, P.R. China*
[3]*Department of Civil and Environmental Engineering, Hong Kong University of Science and Technology, Clear Water Bay, Kowloon, Hong Kong*

(Received July 17, 2015, Revised January 18, 2016, Accepted February 8, 2016)

Abstract. Though hilly topography influences both wind speeds and directions aloft, only the influence on wind speeds, i.e. the speed-up effect, has been thoroughly investigated. Due to the importance of a model showing the spatial variations of wind directions above hilly terrains, it is worthwhile to systematically assess the applicability and limitations of the model describing the influence of hilly topographies on wind directions. Based on wind-tunnel test results, a model, which describes the horizontal and vertical variations of the wind directions separately, has been proposed in a companion paper. CFD (Computational Fluid Dynamics) techniques were employed in the present paper to evaluate the applicability of the proposed model. From the investigation, it has been found that the model is acceptable for describing the vertical variation of wind directions by a shallow hill whose primary-to-secondary axis ratio (aspect ratio) is larger than 1. When the overall hill slope exceeds 20°, the proposed model should be used with caution. When the aspect ratio is less than 1, the proposed model is less accurate in predicting the spatial variation of wind directions in the wake zone in a separated flow. In addition, it has been found that local slope of a hill has significant impact on the applicability of the proposed model. Specifically, the proposed model is only applicable when local slope of a hill varies gradually from 0 (at the hill foot) to the maximum value (at the mid-slope point) and then to 0 (at the hill top).

Keywords: computation; topography; wind characteristics; direction changes

1. Introduction

1.1 Review of previous work

It is evident that the influence of hilly terrains on the wind field in mountainous regions is of importance in both environmental and structural wind engineering. The wind speeds used to calculate wind loads acting on high-rise structures constructed in a mountainous area should take into consideration the wind speed-up effect induced by hilly topography (Miller and Davenport 1998). Particularly, the complex topographic features in Hong Kong has made wind pressures

*Corresponding author, E-mail: li.sunwei@sz.tsinghua.edu.cn

http://www.techno-press.org/?journal=was&subpage=8 ISSN: 1226-6116 (Print), 1598-6225 (Online)

acting on the building erected downstream hilly terrains different from wind pressures acting on buildings constructed on flat terrains (Hitchcock *et al*. 2010). Air pollutant dispersion process is significantly modified by hilly terrain (Jazcilevich *et al*. 2005), and wind resource assessment and wind turbine micro-siting in a mountainous area requires a model describing the influence of hilly terrain on the wind velocity field (Palma *et al*. 2008). Given this importance, developing a model describing the wind field above hilly terrains has been the subject for many previous studies. In a milestone study, Jackson and Hunt (1975) introduced a theory which divides the wind field into two layers, i.e., an inner layer and an outer layer. While the influence of hilly terrain is assumed to be limited into the inner layer, the outer layer is postulated to be inviscid, yielding an analytical description of spatial variations of wind speeds. Following the philosophy of the inner layer theory, Mason and Sykes (1979) extended the work of Jackson and Hunt (1975), and introduced a model describing the wind field perturbed by a three-dimensional shallow hill. The internal boundary layer theory developed by Jackson and Hunt (1975) and Mason and Sykes (1979) formed the basis of a series of more sophisticated models for engineering applications. In particular, Taylor *et al*. (1983) applied the internal boundary layer theory to the wind field above real, complex terrain by describing the terrain in a wave-number space.

Meanwhile, the use of Computational Fluid Dynamics (CFD) techniques in the investigation of the wind field above complex terrains has become popular, along with the growth of computational power and the development of numerical simulation technologies. Due to the scarcity of field measurements and the high cost associated with comprehensive wind-tunnel studies, CFD simulations of wind flows over complex terrains appears to be an appealing alternative for a thorough investigation of topographic influences on the wind field (Bitsuamlak *et al*. 2004). In particular, Bitsuamlak *et al*. (2006) has employed CFD techniques to evaluate the influence of two-dimensional hills on the design wind loads for the structure downstream. Kim, *et al*. (2000) effectively employed CFD techniques to simulate the wind field above the Askervein Hill for which the field measurements are available to compare. Similarly, Balogh *et al*. (2012) conducted a CFD simulation of the wind field above Askervein Hill to validate the proposed turbulence model and wall functions. It is worthwhile mentioning that both studies used the Reynolds-Averaged-Navier-Stokes (RANS) approach and focused on the spatial variation of mean wind speeds above the Askervein Hill. In addition to the RANS simulation, the Large Eddy Simulation (LES) approach has also been adopted in simulating the wind field above complex terrains. Using powerful supercomputers, Uchida and Ohya (2003) simulated the wind field above the new campus of Kyushu University, which is surrounded by complex terrains, using LES techniques.

1.2 The present work

Although many models have been introduced to describe the wind field above hilly terrains, most of them were limited to the influence on the wind speed field, i.e., the speed-up effect. It is well known that the wind flow would also change in direction as a result of the topography. Such influence is, understandably, most significant close to the ground and gradually diminishes aloft. As a result, the wind direction varies vertically. If the yaw angle is defined based on the lateral and longitudinal wind velocities as

$$\theta = \tan\frac{v}{u} \tag{1}$$

the vertical variation of yaw angles reveals the influence of underlying hilly terrains on the wind direction field. In equation (1), θ is the yaw angle, v is the lateral wind velocity and u is the longitudinal wind velocity. In contrast to the speed-up effect, the models describing the vertical variation of yaw angles have rarely been a topic for previous studies. To the best of our knowledge, only the model proposed by Mason and Sykes (1979) and the Engineering Science Data Unit (ESDU 1993) model are publicly available to calculate the spatial variations of yaw angles. The model introduced by Mason and Sykes (1979) is too complicated to be applied as an engineering model, and the applicability and the limitations of the ESDU model has not been systematically discussed.

In a companion paper (Weerasuriya *et al*. 2016), a model is proposed to describe the vertical variation of yaw angles induced by a three-dimensional hill with idealized geometries. While the proposed model postulates that the vertical variations of longitudinal ($u(z)$) and lateral ($v(z)$) wind velocities are linearly related in a hill-perturbed wind field in the form

$$v(z) = c_1 u(z) + c_2 \tag{2}$$

the input parameters c_1 and c_2 are determined through the critical longitudinal (u_c) and lateral (v_c) velocities as

$$v_c = c_1 u_{surf} + c_2 \tag{3}$$

$$u_c = \frac{-c_2}{c_1} \tag{4}$$

The horizontal variations of u_c and v_c are, on the other hand, calculated based on the geometry of the hill as

$$s_v = \frac{v_c/V}{(dz/dy)_{0,y}} \tag{5}$$

$$\begin{cases} \dfrac{s_v}{s_{vmax}} = \exp\left[-\left(\dfrac{x}{L_1}+1\right)^2\right] & \dfrac{x}{L_1} < -1 \\ \dfrac{s_v}{s_{vmax}} = \sin\left(-\dfrac{\pi}{2}\dfrac{x}{L_1}\right) & -1 < \dfrac{x}{L_1} < 0 \\ \dfrac{s_v}{-0.8 s_{vmax}} = \sin\left(\dfrac{\pi}{2}\dfrac{x}{1.2L_1}\right) & 0 < \dfrac{x}{1.2L_1} < 1 \\ \dfrac{s_v}{-0.8 s_{vmax}} = \exp\left[-\left(\dfrac{x}{L_1}-1.2\right)^2\right] & \dfrac{x}{1.2L_1} > 1 \end{cases} \tag{6}$$

In Eq. (3), u_{surf} is the longitudinal wind velocity at the near-surface level (5 m from the local ground as suggested in the companion paper –Weerasuriya *et al*. 2016). In Eq. (5), $(dz/dy)_{0,y}$ is the local hill slope along the lateral centerline of the hill, V is the unperturbed, total wind speed at the same level as v_c. In Eq. (6), s_{vmax} is the maximum lateral perturbation parameter and L_1 is the characteristic length scale of the hill model in the longitudinal direction. For the details of the proposed model, the readers are advised to refer to the companion paper. Based on the wind-tunnel experiment results, the reliability and accuracy of the proposed model is first evaluated. It has been found that, although the linear relationship between longitudinal and lateral wind velocities is valid for the hill models been tested, the applicability of Eqs. (5) and (6) has boundaries. Due to the limits of wind-tunnel measurements, the applicability and limitations of the proposed model can not be further discussed in the companion paper. As a supplement to the wind-tunnel experiments,

a series of CFD simulations were conducted to assess the applicability of the proposed model under various conditions in the present paper.

Section 2 presents the validation of the CFD simulation by comparing CFD simulation results to the wind-tunnel model measurements, which includes a brief discussion on the impacts of using "stepped" hill models in the wind-tunnel experiments. Using the CFD simulation results corresponding to hills with different geometries, Section 3 discusses the applicability and limitations of the proposed model. The conclusions are listed in Section 4.

2. CFD simulation validation

2.1 General approach and grid dependency

Before the CFD simulations can be utilized to investigate the applicability and limitations of the proposed model, it is necessary to first verify that the CFD simulation is a reliable supplement to the wind-tunnel experiment. Therefore, a CFD simulation of the wind field perturbed by the numerical replica of the hill model used in the wind-tunnel experiment was carried out, yielding results comparable to the wind-tunnel measurements. In detail, the CFD simulation was based on OpenFOAM-2.3 and employed the SIMPLE algorithm to solve the Reynolds-Averaged Navier Stokes equations. The computational domain was $23\ \mathrm{m} \times 13\ \mathrm{m} \times 2\ \mathrm{m}$ ($\mathrm{length} \times \mathrm{width} \times \mathrm{height}$). It should be pointed out that the hill model employed in the wind-tunnel experiment, detailed in the companion paper, is a "stepped" model, which was manufactured by accumulating layers of foam sheets. The hill elevation (z) can be calculated according to the horizontal location (x, y) as

$$z = \frac{H}{2} + \frac{H}{2} cos\left(\frac{\pi}{2L_1}\sqrt{x^2 + Ay^2}\right) \tag{7}$$

In Eq. (7), H is the hill height, which takes the value of $200\ \mathrm{mm}$ and A is the aspect ratio of the hill, which takes the value of 1. The mesh was set up according to the shape of the "stepped" hill model. In the vertical direction, half of the step size (2.5 mm) of the wind-tunnel hill model was used to discretize the space adjacently above the hill. From the boundaries of the domain to the hill model, which is located at the domain center, the grid size gradually decreased to a value close to $2.5\ \mathrm{mm}$ in the horizontal plane. Fig. 1 presents two views of the grid system around the hill model. It is reasonable to speculate that the grid spacing, especially in the vertical direction, would impact the simulation results. Consequently, a grid independency test was conducted through conducting same simulations with finer grid systems. In detail, while the horizontal meshing scheme remains unchanged, the grid spacing in the vertical direction near the "stepped" hill model reduced to $1/4$ of the step size ($1.25\ \mathrm{mm}$). As a result, the total cell number increases from 0.87 million to 1.74 million. In order to show the influence of hill geometries on the grid independency, hill models with aspect ratios of $1/3$, $1/2$, 2 and 3 were included in the simulations with the original and finer grid systems. Through comparing the near-surface longitudinal and lateral wind velocities extracted from the original simulation (u_{org} and v_{org}) and the simulation with finer grid (u_{fin} and v_{fin}), a grid independency test was carried out. In detail, the differences between u_{fin} and u_{org} and between v_{fin} and v_{org} are squared to show how close the results from the simulation with finer grid system is to the results from the original simulation. Table 1 summarizes the mean of the squared differences in different grid independency

checks. Considering the total wind velocity at the near-surface level is around $6\ \mathrm{m/s}$, the squared differences reported in Table 1 can be seen to be acceptable. In other words, the comparative results reported in Table 1 indicate the results from the original simulation are grid independent.

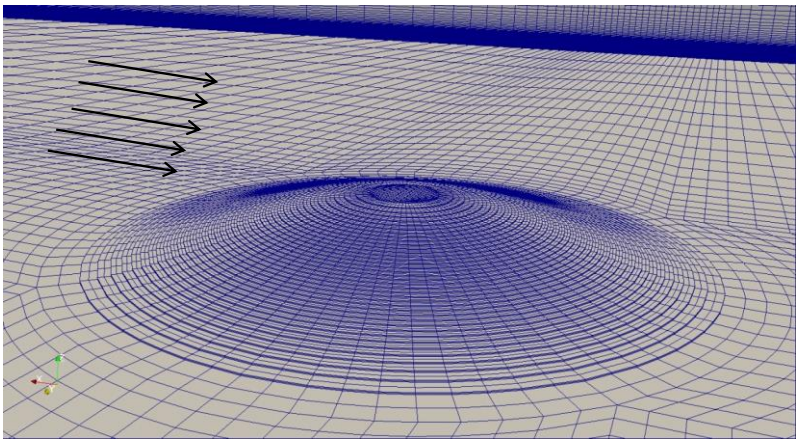

(a)

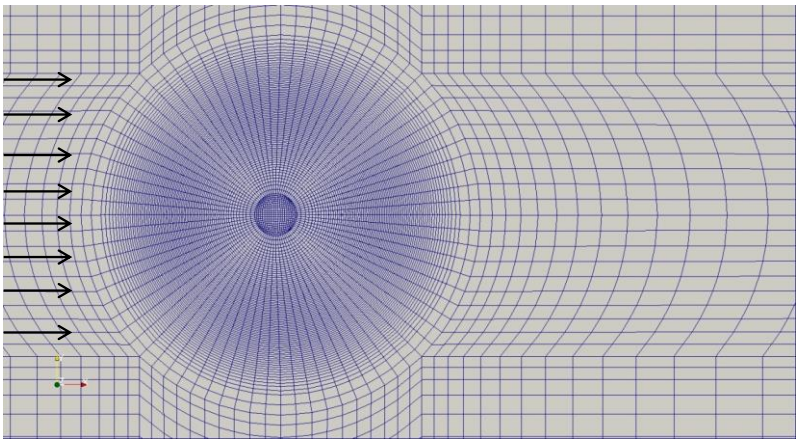

(b)

Fig. 1 The grid system in the CFD simulation of the stepped hill model. The grid system is presented from two perspectives. The approaching wind flow is indicated by the array of arrows

Table 1 The grid independency check results

Aspect ratio	$1/3$	$1/2$	1	2	3
$\overline{(u_{org} - u_{fin})^2}$	0.1062	0.0571	0.0182	0.0257	0.0301
$\overline{(v_{org} - v_{fin})^2}$	0.0267	0.0056	0.0004	0.0002	0.0001

2.2 Boundary conditions

For the purpose of validation, the inflow boundary conditions of the CFD simulation should be an acceptable approximation of the approaching wind flow calibrated in the wind-tunnel experiment. Therefore, the target mean velocity and turbulence intensity profiles used in the wind–tunnel experiment to calibrate the approaching wind flow were adopted to specify the inflow boundary conditions of the longitudinal wind velocity (u) and the turbulent kinetic energy (k) in the CFD simulation. Although the inflow boundary conditions of u and k can be specified exactly as the desired profiles, the sustainability of the inflow requires that the mean velocity profile follows the log-law model and the turbulent kinetic energy profile follows the equations provided by Yang *et al*. (2009). In detail, the friction velocity (u_*) and aerodynamic roughness length (z_0) were derived by fitting the desired mean wind profile to the log-law model. The results ($u_* = 0.30\ m/s$ and $z_0 = 1.08 \times 10^{-4}$m) were then used to calculate the profile of k following the equations provided by Yang *et al*. (2009). In order to check the sustainability of the inlet boundary conditions specified as above, a separate simulation was conducted with the same inlet boundary conditions of u and k specified at the inlet of an empty domain. In detail, the empty domain has the same dimension as the original simulation. The "stepped" hill model was, however, absent.

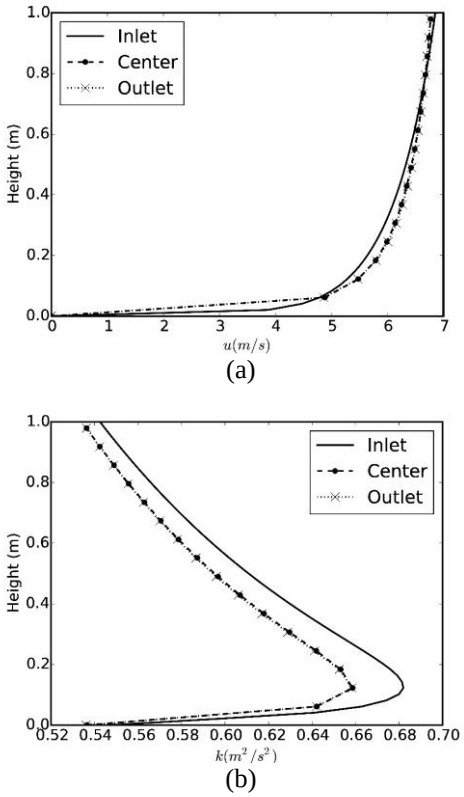

Fig. 2 Comparisons of u and k profiles at the inlet, the middle (center) and the outlet of the empty domain to check the sustainability of the inlet profiles

Therefore, the profile sustainability could be evaluated through comparing the profiles of u and k extracted from the middle and the outlet of the domain to the inlet profiles. Fig. 2 shows such profile comparisons. It is evident from the figure that both the profiles of u and k were successfully sustained throughout the empty domain. Thus, it is reliable to employ the inlet profiles shown in Fig. 2 to conduct the CFD simulations with the hill models.

As for other boundary conditions, a symmetry condition was employed for the lateral boundaries, the slip condition was employed for the top boundary, the pressure at the outlet was assumed to be constant and the wall condition was specified for the ground and the surface of the hill model. When comparing the CFD simulation results to the wind-tunnel measurements, it has been found that the standard wall function is inadequate to yield the observed lateral wind perturbations. Consequently, the wall function was revised to explicitly include the manually specified aerodynamic roughness length in the calculation of the shear stresses at the wall, and the value of the aerodynamic roughness length was specified according to fitting the approaching mean wind profile to the log-law model ($z_0 = 1.08 \times 10^{-4}$m).

2.3 Other numerical set-ups

Besides the boundary conditions, other numerical set-ups are also critical for the simulation of wind field above topographic features. To be more specific, the turbulence model, the discretization scheme for the convection term and criteria for the convergence check are primitive for the success of a CFD simulation.

In the present study, the $k-\varepsilon$ model was used to parameterize the turbulent diffusion that should be taken into consideration when solving the RANS equations. In fact, the turbulent viscosity appeared in the RANS equations should be calculated by an additional model which depends on the solved fluid field variables. Although the LES technique is also useful in simulating the topography-perturbed wind field (Uchida and Ohya 2003), the computational burden associated with the LES make it is not worthwhile to be employed in a study focusing on the wind field characteristics at a scale comparable to a hill (~1 km). Under the condition that the RANS simulation is adopted, both the $k-\omega$ model and the $k-\varepsilon$ model are frequently used. While the $k-\omega$ model is more suitable for the simulation of the wind field perturbed by a bluff body, the $k-\varepsilon$ mode has been recognized as appropriate for simulations in a wider range (Tominaga *et al*. 2008).

For the discretization scheme for the convection term in the momentum equation, the QUICK scheme was utilized. Such scheme calculates the velocity derivatives according to three solved velocities (two upstream and one downstream). Such a scheme is second-order in accuracy and is more stable when comparing to other second-order discretization scheme. For discretizing other terms in the momentum equation, the linear scheme is employed. It should be pointed out that the linear scheme is also a second-order scheme. It is less stable comparing to the QUICK scheme but requires less computational power.

The simulations are conducted through solving the RANS equation iteratively. The relaxation factor employed in the iteration is 0.3 for the pressure and 0.7 for other variables. The convergence is considered achieved, and hence the iteration is stopped, once the relative residuals between two successively iteration all reduced to 0.001. It should be noted that all simulations under investigation converged before the iteration limit of 6000.

2.4 Comparison with wind-tunnel results

Since the aim of the CFD simulation is to evaluate the proposed model, the near-surface yaw angle (θ_{surf}) simulated by CFD is compared with the wind-tunnel observed values in Fig. 3. The near-surface yaw angle is defined as the yaw angle simulated/measured at the height of 10 mm in the model scale (5 m in the full scale). It is clear that the contours of θ_{surf} calculated from the CFD simulation are in an acceptable agreement with the contours calculated based on the wind-tunnel measurements. More specifically, both the CFD simulated and wind-tunnel measured maximum and minimum θ_{surf} are located approximately at the same location. The contours calculated from the wind-tunnel measurements are, however, not as symmetric as the contours calculated from the CFD simulation results about the axis of $y = 0$. In order to be more illustrative, the differences between wind velocities derived from the CFD simulation results and the wind-tunnel measurements are calculated in addition to θ_{surf}. Fig. 4 shows the vertical profiles of mean velocity differences (u and v) calculated by averaging the absolute velocity differences at the heights where the wind-tunnel measurements area available.

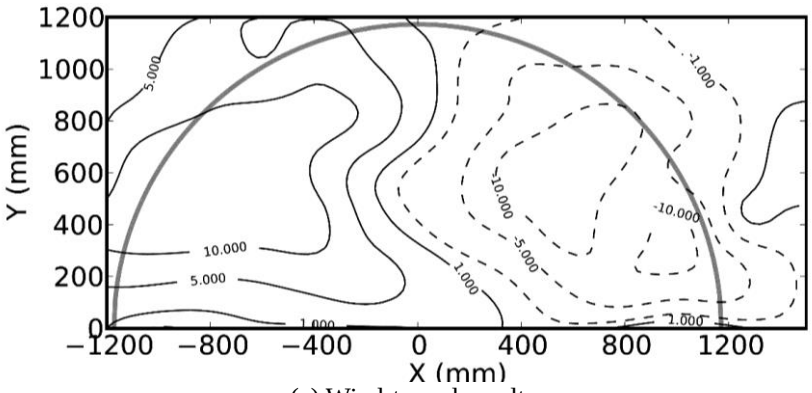

(a) Wind-tunnel results

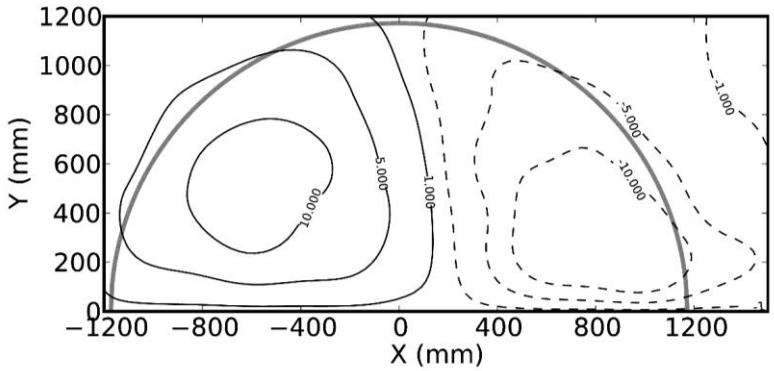

(b) CFD simulation

Fig. 3 The comparison of the near-surface yaw angle (θ_{surf}) in the wind-tunnel test and derived from the CFD simulation results

In other words, the differences between the wind-tunnel measured and the CFD simulated longitudinal and lateral wind velocities at the same level were calculated. The differences were then averaged to show as data points in Fig. 4. Connecting all the data points corresponding to different levels produces the vertical lines.

From Fig. 4, it is clear that the velocity difference of u decreases vertically and the velocity difference of v roughly keeps a constant in the vertical direction. In fact, the velocity differences of u and v are in the range of $0.2\sim0.7\ \mathrm{m/s}$ and $0.06\sim0.14\mathrm{m/s}$. The longitudinal and lateral wind velocities observed in the wind-tunnel test were, however, approximately $6\ \mathrm{m/s}$ and $1.2\ \mathrm{m/s}$ in the region where the vertical variation of wind directions is significant ($\theta_{surf} > 5°$). Consequently, the CFD simulation is shown to be valid in terms of simulating the wind field perturbed by a "stepped" hill model.

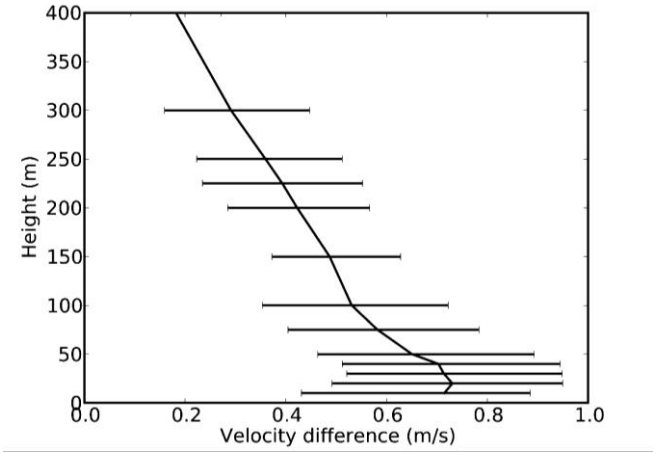

(a) u

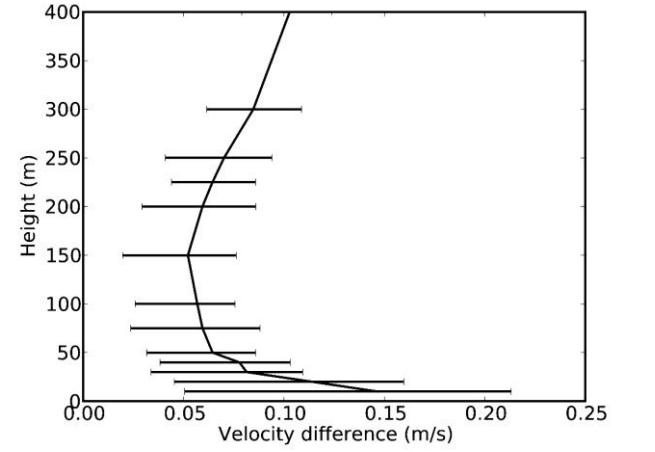

(b) v

Fig. 4 The vertical variations of the wind velocity differences between CFD simulated and wind-tunnel measured u and v. The error bars indicate the 25% and 75% percentiles

Theoretically, both the wind-tunnel test and the CFD simulation should be conducted using a hill model with smoothed surfaces, because the "stepped" hill is clearly not a completely realistic representation of real topography. The reason for employing a "stepped" hill model in the wind-tunnel test is to promote Reynolds number independence (Derickson and Peterka 2004). Although it has been shown that a carefully selected step size can make the wind-tunnel simulation acceptably approximate the real-terrain-perturbed wind field, such a conclusion has been derived based mainly upon the investigation on the wind speed field. Whether the use of "stepped" hill models is appropriate in a wind-tunnel study including direction changes is a question to be answered. In order to verify the use of a "stepped" hill model, a series of CFD simulations should be conducted to reveal how the wind field perturbed by a "stepped" hill at the model scale is compared to the wind field perturbed by "smoothed" hills at the model scale and at the full scale. As a result, two more CFD simulations, in which the "smoothed" hills at the model scale and at the full scale were included, have been conducted in addition to the simulation employed for validation.

While the computation method corresponding to the "smoothed" hill at the model scale is similar to that for the "stepped" hill case, the simulations corresponding to the full scale were scaled up by the geometric scale used in the wind-tunnel experiment ($1{:}\,500$). In the simulations of the "smoothed" hills, the size of the cells near ground is no longer restricted by the step size of the hill model. In fact, the hill surface was modelled as continuously smooth face, and hence the mesh covered the hill as if it were a flat plane. Fig. 5 shows the horizontal grid near the "smoothed" hill model. The averaged cell size in the horizontal planes, on the other hand, approximately equals the averaged horizontal grid spacing in the "stepped" hill case when the geometric scale is taken into consideration (5 mm in the model scale and 2.5m in the full scale). The cell sizes in the vertical direction, on the other hand, increase gradually from 3 mm to 105 mm for the model-scale model and from 1.5 m to 53 m for the full-scale hill.

The boundary conditions of the additional simulations were copied from the "stepped" hill model case, except for the inflow and wall boundary conditions in the simulation corresponding to the full-scale hill. More specifically, the desired mean velocity profile utilized in the wind-tunnel test was scaled up by the geometric scale of the wind-tunnel experiment ($1{:}\,500$), based on which the updated friction velocity and aerodynamic roughness length were derived ($u_* = 0.3$ m/s,$z_0 = 0.054$ m). While the inflow profiles of u and k were calculated based on the updated log-law model parameters, the aerodynamic roughness length used by the wall function in the simulation with the full-scale hill was specified following the suggestion of for the grass exposure ($z_0 = 0.03$ m) .

As the topic of present study is the vertical variation of wind directions induced by hilly topographies, the near-surface yaw angles calculated based on the CFD simulations corresponding to the "stepped" hill model, the "smoothed" hill model and the full-scale hill are compared in Fig. 6. It is clear from the comparison that the horizontal variations of the near-surface yaw angles calculated from different CFD simulations are generally in agreement. More importantly, whilst the near-surface yaw angles produced by the simulations corresponding to the "stepped" hill model and the full-scale hill are in good agreement, the near-surface yaw angles calculated from the simulation of the "smoothed" hill model has been found smaller than the results of the other simulations. In order to show the influence of the "stepped" hill model in a more illustrative way, the simulations of the near-surface u and v were compared in Figs. 7 and 8. From the comparisons, it has been found that the near-surface v contours produced by the simulations corresponding to the "smoothed" hill model and the full-scale hill are in better agreement among

the three simulations. The near-surface u contours, on the other hand, produced by the simulation of the full-scale hill are in better agreement with the simulations results corresponding to the "stepped" hill model. From Figs 7 and 8, it can be discerned that the use of the "stepped" hill model in wind-tunnel experiments yields a better simulation of the longitudinal wind velocity above the hill as revealed by previous studies (Lindley *et al*. 1981, Lubitz and White 2007). The reduced-scale-simulation of the lateral wind velocity, on the other hand, is not improved by using the "stepped" hill model. Nevertheless, the overall simulation of the vertical variation of wind directions in the wind-tunnel is improved through using the "stepped" model as an accurate description of the twist effect certainly depends on the spatial variation of the longitudinal wind velocity, u.

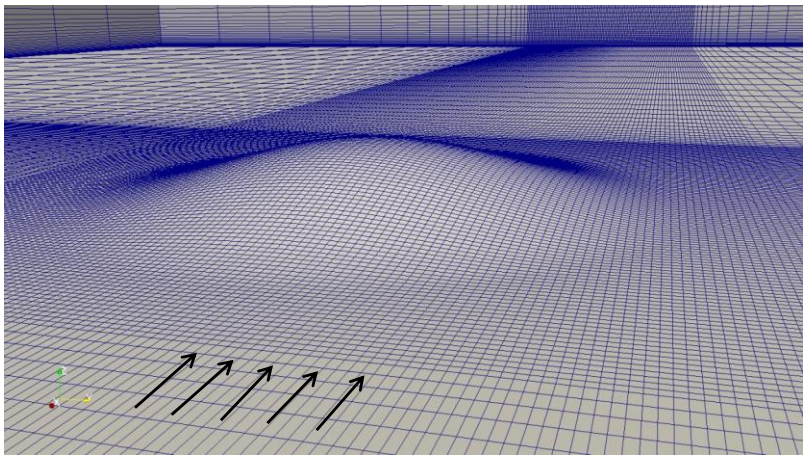

(a)

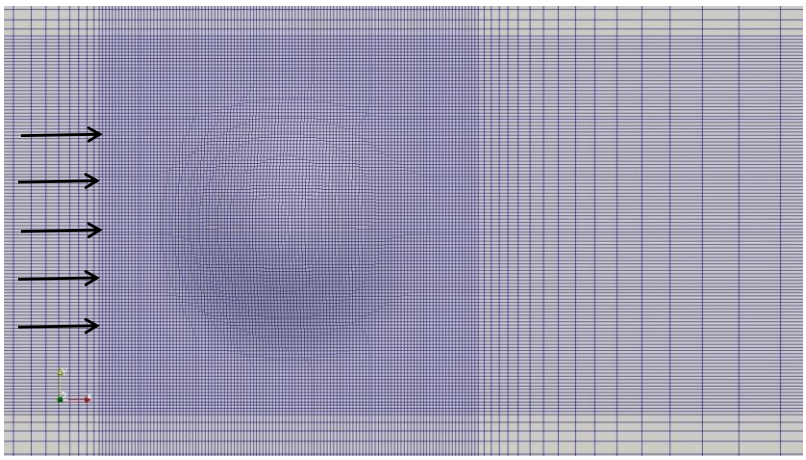

(b)

Fig. 5 The grid system in the CFD simulation of the smoothed hill model. The grid system is presented from two perspectives. The approaching wind flow is indicated by the array of arrows

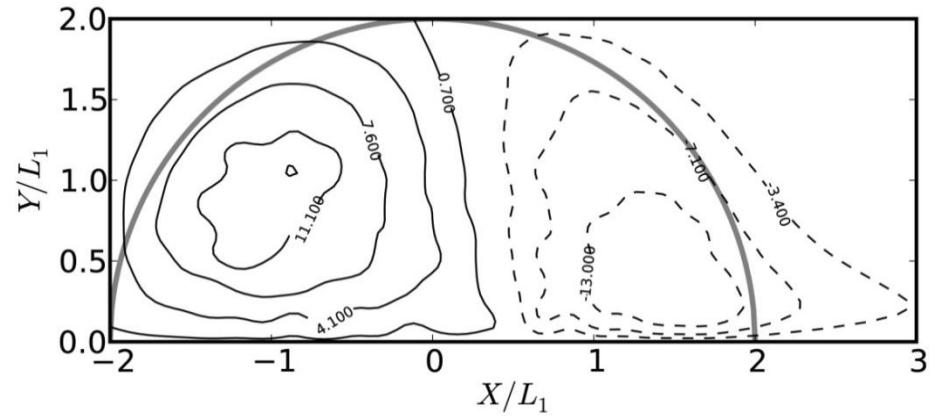

(a) Stepped hill model

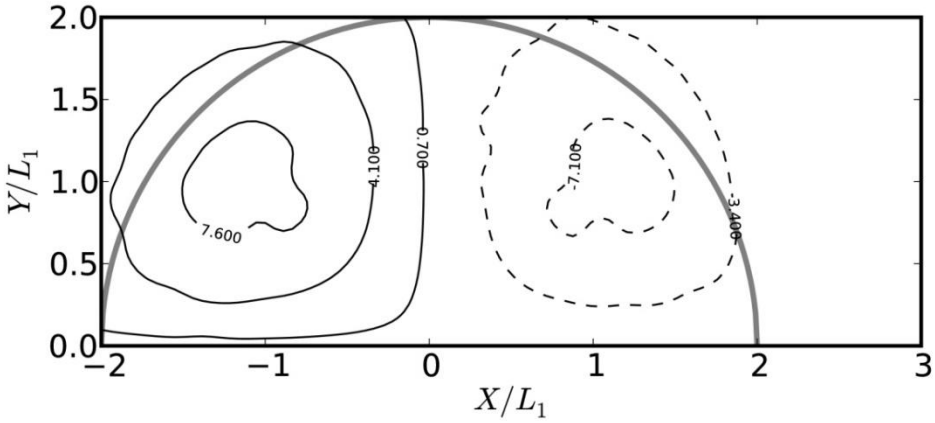

(b) Smooth hill model

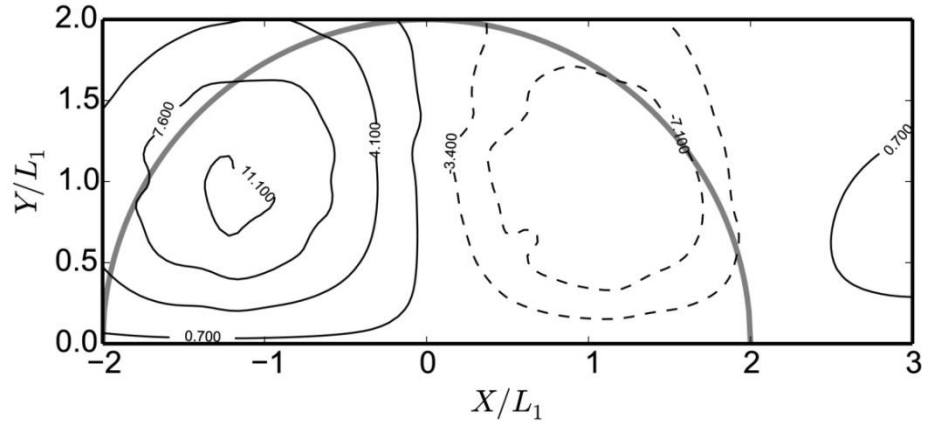

(c) Full-scale hill

Fig. 6 Comparison of near-surface yaw angles (θ_{surf}) calculated based on the CFD simulation results of the stepped model, the smoothed model and the full-scale model

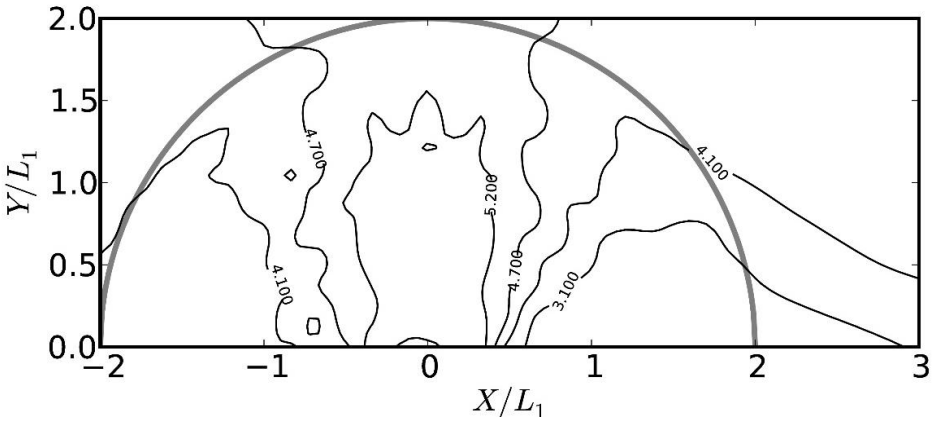

(a) Stepped model

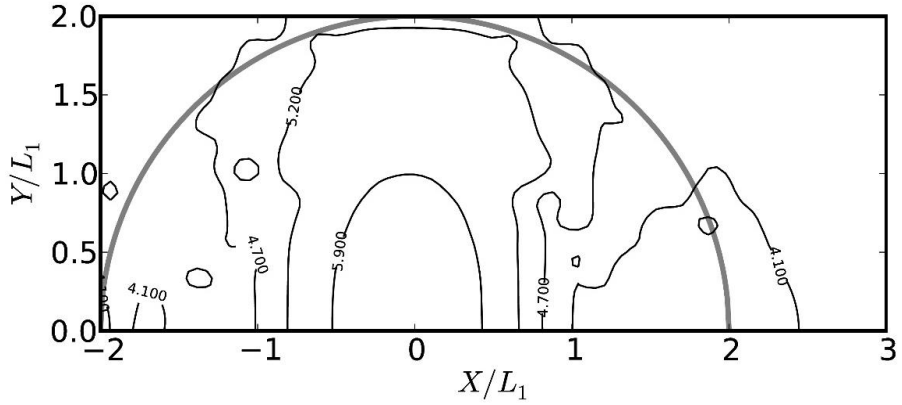

(b) Smooth model

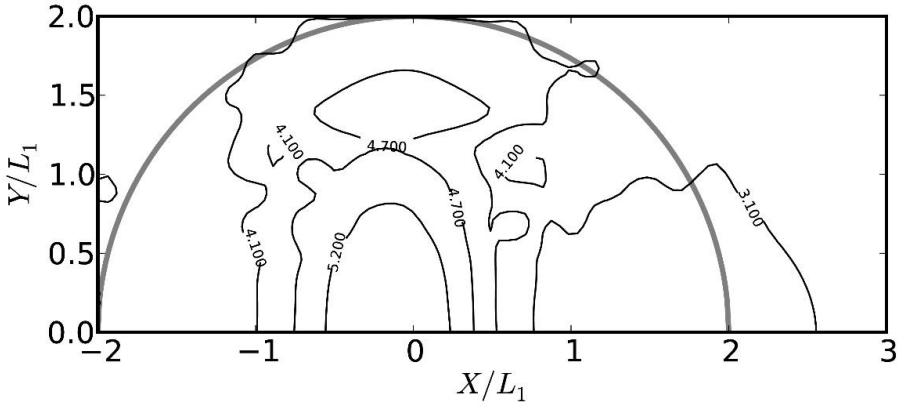

(c) Full-scale model

Fig. 7 Comparison of the longitudinal wind velocity (u) calculated based on the CFD simulations results of the stepped model, the smoothed model and the full-scale model

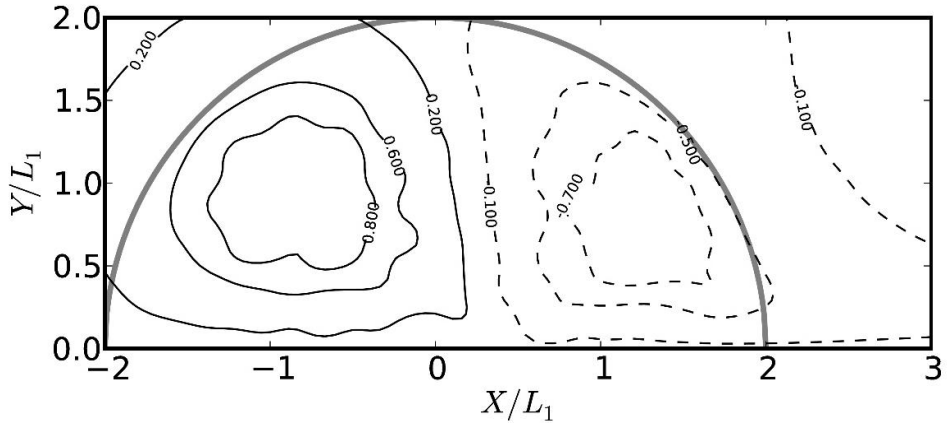

(a) Step model

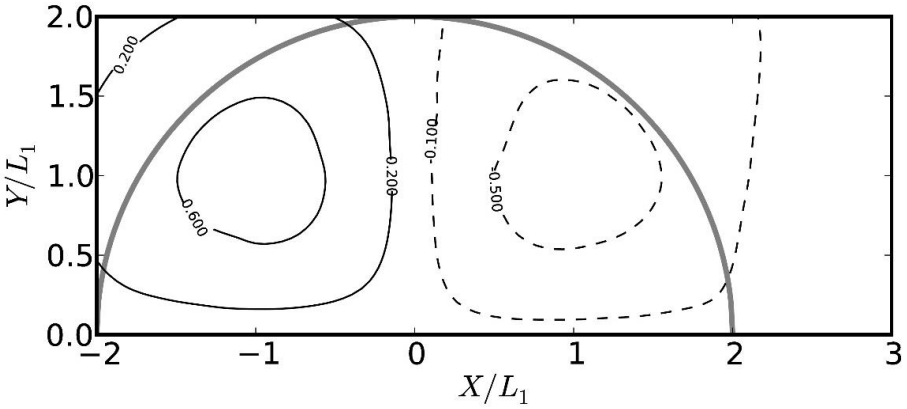

(b) Smooth model

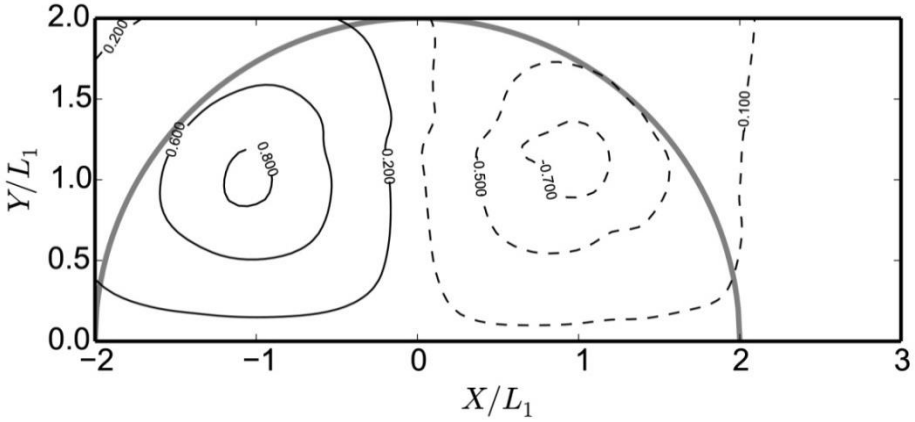

(c) Full Scale model

Fig. 8 Comparison of the lateral wind velocity (v) calculated based on the CFD simulation results of the stepped model, the smoothed model and the full-scale model

3. Applicability and limitations of the proposed model

3.1 Vertical variation of lateral wind velocities

In the proposed model, the vertical variation of yaw angles was calculated based on the vertical variations of longitudinal and lateral wind velocities, which are correlated through a linear function (Eq. (2)). Given the total wind velocity, which can be derived from a model describing on the speed-up effect, Eq. (2) indirectly specifies the vertical variation of yaw angles.

Unlike an empirical model, Eq. (2) is derivable from the Reynolds-averaged Navier-Stokes equations under a series of conditions. Specifically, the momentum equations of the longitudinal and lateral wind velocities are

$$u_j \frac{\partial u_1}{\partial x_j} = -\frac{1}{\rho}\frac{\partial p}{\partial x_1} + \frac{\partial}{\partial x_j}\left[\upsilon_t\left(\frac{\partial u_1}{\partial x_j} + \frac{\partial u_j}{\partial x_1}\right)\right] \tag{8}$$

$$u_j \frac{\partial u_2}{\partial x_j} = -\frac{1}{\rho}\frac{\partial p}{\partial x_2} + \frac{\partial}{\partial x_j}\left[\upsilon_t\left(\frac{\partial u_2}{\partial x_j} + \frac{\partial u_j}{\partial x_2}\right)\right] \tag{9}$$

In Eqs. (8) and (9), the Einstein notation is implied and the wind velocity components u, v and w is replaced by the tensor notation of (u_1, u_2, u_3). Similarly, the coordinates x, y and z is replaced by the tensor coordinates (x_1, x_2, x_3). Moreover, ρ is the air density, υ_t is the turbulent viscosity calculated by a turbulence model. If the horizontal variations of u and v, or u_1 and u_2, are negligibly small comparing to the vertical variations of u and v (u_1 and u_2), Eqs. (8) and (9) can be reduced to

$$u_3 \frac{\partial u_1}{\partial x_3} = \frac{\partial}{\partial x_3}\left[\upsilon_t\left(\frac{\partial u_1}{\partial x_3}\right)\right] \tag{10}$$

$$u_3 \frac{\partial u_2}{\partial x_3} = \frac{\partial}{\partial x_3}\left[\upsilon_t\left(\frac{\partial u_2}{\partial x_3}\right)\right] \tag{11}$$

because $\partial/\partial x_1 \approx 0$ and $\partial/\partial x_2 \approx 0$. Due to the similarity between Eqs. (10) and (11), it follows that the lateral wind velocity v should be in a linear relationship with longitudinal wind velocity u. In that case, Eqs. (10) and (11) essentially reduce to one equation concerning only the longitudinal wind velocity u. From the derivation shown above, it can be concluded that Eq. (2) is consistent with the Reynolds-averaged Navier Stokes equations, given the horizontal variation of both longitudinal and lateral wind velocities are negligibly small comparing to their vertical variations.

In order to reveal the dependency of the validity of Eq. (2) on the horizontal homogeneous assumption in a more direct way, two indicators are employed, namely the absolute correlation coefficient and the gradient ratio. While the absolute correlation coefficient between v and u shows the validity of Eq. (2), the gradient ratio indicates how the horizontal variations of u and v compare to their vertical variations. More specifically, the absolute correlation coefficient was calculated as

$$\rho_{uv} = \left|\frac{E[(u-Eu)(v-Ev)]}{\sigma_u \sigma_v}\right| \tag{12}$$

and the gradient ratio was calculated as

$$r = \frac{\sqrt{\left(\frac{\partial u}{\partial x}\right)^2 + \left(\frac{\partial v}{\partial x}\right)^2 + \left(\frac{\partial u}{\partial y}\right)^2 + \left(\frac{\partial v}{\partial y}\right)^2}}{2\sqrt{\left(\frac{\partial u}{\partial z}\right)^2 + \left(\frac{\partial v}{\partial z}\right)^2}} \tag{13}$$

In Eqs. (12) and (13), u is the longitudinal wind velocity, v is the lateral wind velocity, Eu, Ev denote the mean values of u and v in a vertical profile and σ_u, σ_v denote the standard deviations of u and v in the same vertical profile.

Fig. 9 presents the contours of the absolute correlation coefficient (ρ_{uv}) and the gradient ratio (r). It is clear from this figure that there is coherent relation between ρ_{uv} and r. A small value of r coincides with ρ_{uv} being approximately equal to 1, especially in the regions at some distances from the hill. In the region near the peak of the hill, although r is small ($r < 0.04$), ρ_{uv} deviates from 1 by a value in the range of 0.4~0.6. Since the value of v is small in the peak region due to the symmetry of the wind field in the lateral direction, ρ_{uv} in the peak region is extremely sensitive to the value of v. In other words, ρ_{uv} is no longer a suitable indicator to show the validity of Eq. (2) in the hill peak region. Furthermore, the assessment of the validity of Eq. (2) in the hill peak region is somewhat pointless as the lateral wind velocity, and hence the vertical variation of yaw angles, is negligible in the hill peak region.

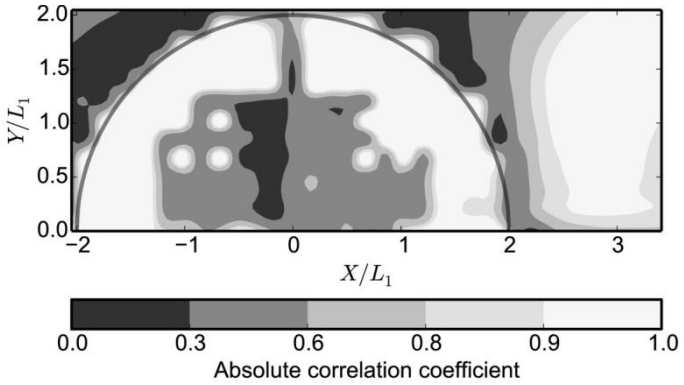

(a)

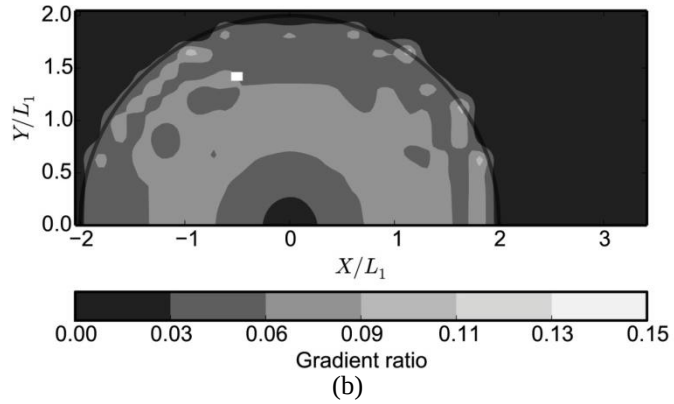

(b)

Fig. 9 Contours of the absolute correlation coefficient and the gradient ratio, calculated based on the CFD simulation of the full-scale model (the aspect ratio of 1 and the hill height of 100 m)

As the dependency of ρ_{uv} on r has validated the use of gradient ratios to indicate whether Eq. (2) is applicable to calculate the vertical variation of yaw angles, the gradient ratios calculated based on the CFD simulation of hills with different geometries are presented and discussed. Specifically, the aspect ratio and the height of the hill vary to simulate hills with different geometries. Fig. 10 presents the contours of gradient ratios calculated based on the CFD simulations of the hills with the aspect ratios of $1/2$ and 2. By comparing Fig. 10(a) to Fig. 9(b) and Fig. 10(b), it is found that the gradient ratio reaches the minimum when the hill aspect ratio equals 1. In the cases where the aspect ratio of the hill is 2 or $1/2$, the gradient ratio slightly increases. In order to show the influence of the hill aspect ratio in a quantitative manner, the averaged gradient ratios and the averaged absolute correlation coefficients corresponding to the hills with different aspect ratios are summarized in Table 2. It is clear from the table that the averaged ρ_{uv} reaches maximum and the averaged r reaches minimum when the hill aspect ratio equals 1. Therefore, it can be concluded that Eq. (2) is less applicable when there is a primary axis in the hill (in either the longitudinal or the lateral direction).

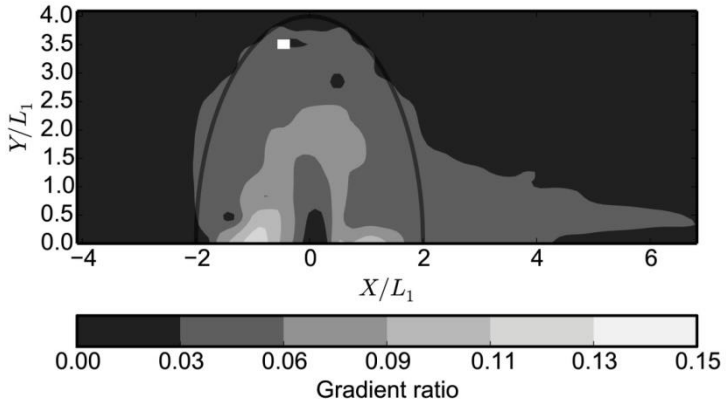

(a) $A = 1/2$

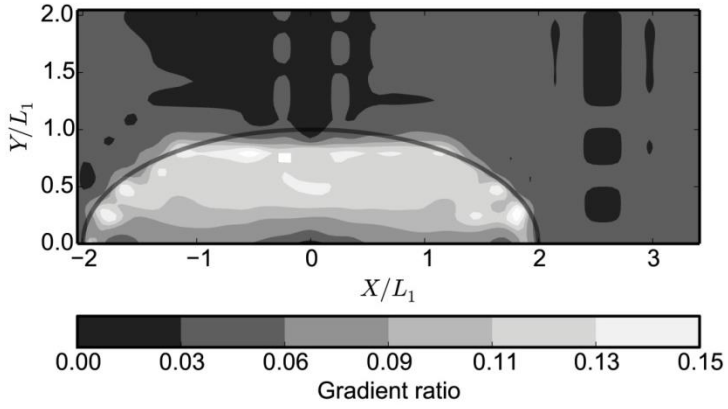

(b) $A = 2$

Fig. 10 Contours of gradient ratios calculated based on the CFD simulations of the full-scale hill models with the aspect ratios of $1/2$ and 2

Table 2 The averaged absolute correlation coefficients and gradient ratios corresponding to different hill aspect ratios

Aspect ratio	$^1/_3$	$^1/_2$	1	2	3
ρ_{mean}	0.617	0.714	0.804	0.680	0.589
r_{mean}	0.055	0.056	0.038	0.052	0.050

Table 3 Averaged absolute correlation coefficients and gradient ratios corresponding to different hill overall slopes

Hill height	100 m	150 m	200 m	250 m	300 m
Overall slope	9.68°	14.35°	18.83°	23.10°	27.10°
ρ_{mean}	0.804	0.802	0.738	0.580	0.493
r_{mean}	0.038	0.060	0.087	0.125	0.132

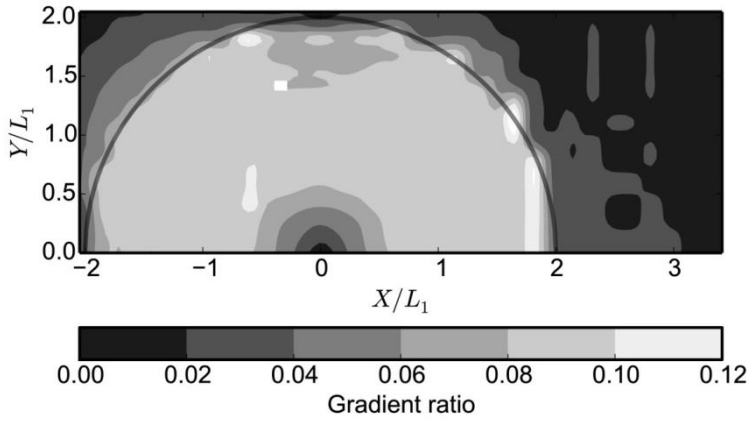

(a) H = 150 m

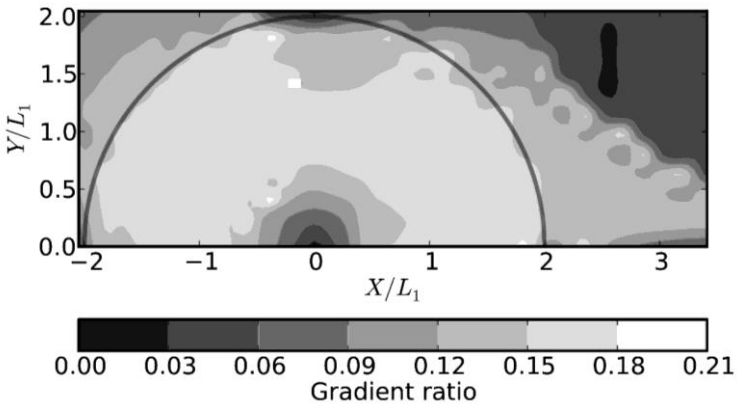

(b) H = 250 m

Fig. 11 Contours of gradient ratios calculated based on the CFD simulation results of the hill models with the hill heights of 150 m and 250 m

In addition to the aspect ratio, the hill height was varied from 150 m to 300 m in the CFD simulation to investigate the influence of the overall hill slope on the applicability of Equation (2). Fig. 11 presents the contours of gradient ratios calculated based on the CFD simulations corresponding to the hills with heights of 150 m and 250 m. Apparently, the hill height has more significant impacts on the gradient ratio than the aspect ratio of the hill. As expected, the gradient ratio increases, in general, with the hill height. In the case where the hill height equals 150 m, the gradient ratio was found less than 0.1 for the majority portion of the wind field. In the case where the hill height equals 250 m, the gradient ratio is larger than 0.18 in an area covering the hill (expect for the hill peak). Since the characteristic length scale of the hill at a horizontal plane was fixed in the CFD simulation, the increase of the hill height actually implies an increase of the overall hill slope. Consequently, it is argued that the increase of the gradient ratio is due to the increase of the hill slope. As in the investigation on the influence of the aspect ratio, the averaged gradient ratios and absolute correlation coefficients corresponding to the hill heights of 100 m, 150 m, 200 m, 250 m, 300 m are summarized in Table 3, which shows that the applicability of Eq. (2) reduces with the increase of the hill height, and hence the increase of the overall slope of the hill. In fact, when the overall hill slope exceeds 20°, it is suggested that Eq. (2) should be used with caution.

3.2 Horizontal variation of model parameters

A key concept employed by the proposed model is the introduction of the lateral perturbation parameter. According to the proposed model, the lateral perturbation parameter, which is assumed to be constant in the lateral direction, is calculated based on the near-surface lateral wind velocity and the local hill slope along the lateral centerline (Eq. (5)). Using the CFD simulation results corresponding to the hills with different geometries, two factors are investigated, namely the lateral variations of the lateral perturbation parameter and the applicability of Eq. (6) in describing the longitudinal variations of lateral perturbation parameters.

Calculating the lateral perturbation parameters using the CFD simulated u and v at near-surface level (5 m from the local ground), both the longitudinal and lateral variation of the lateral perturbation parameter can be investigated. For the sake of simplicity, two auxiliary parameters are introduced, namely the normalized lateral perturbation parameter ($s_v{}^r$) and the normalized x coordinate (x^r). The definitions of $s_v{}^r$ and x^r are

$$\begin{cases} s_v{}^r = \frac{s_v}{s_{vmax}} & x < 0 \\ s_v{}^r = \frac{s_v}{0.8 s_{vmax}} & x > 0 \end{cases} \tag{14}$$

$$\begin{cases} x^r = \frac{x}{L_1} & x < 0 \\ x^r = \frac{x}{1.2 L_1} & x > 0 \end{cases} \tag{15}$$

With the help of the definitions of $s_v{}^r$ and x^r, it is easy to discern that $s_v{}^r$ is a simple exponential-sine function of x^r according to Eq. (6). Fig. 12 presents the variations of $s_v{}^r$ with x^r calculated based on the CFD simulation results at lines parallel to the longitudinal centerline of the hill. Clearly, Fig. 12 indicates that Eq. (6) is acceptable in terms of modelling the horizontal variations of the direction changes. Especially in the windward zone, the scattered points

calculated based on the CFD simulation results agree, to an acceptable extent, with the theoretical curve calculated according to Eq. (6). In the wake zone ($x^r > 0$), the scattered points, calculated based on the CFD simulations, slightly deviate from the theoretical curve. Specifically, the peak of the scattered points is shifted to the left when compared with the theoretical curve. Since the CFD simulation has been found less reliable in the wake zone when comparing to the wind-tunnel test result, such a deviation may imply the deficiency of the CFD simulation rather than the inaccuracy of the model. Consequently, the investigation on the applicability and limitations of the model in describing the horizontal variation of the direction changes focuses on the windward zone.

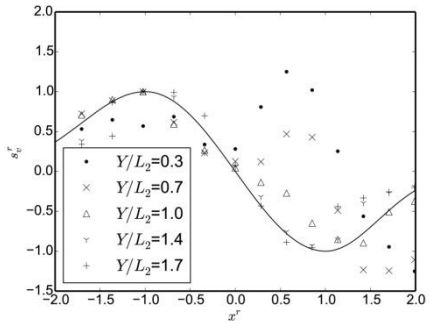

(a) $A = 1/2$

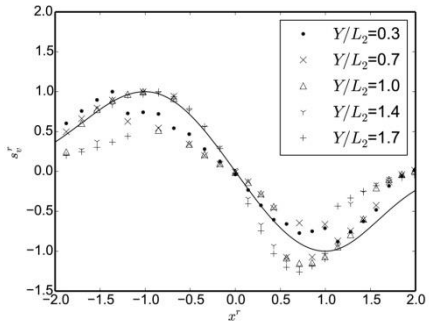

(b) $A = 1$

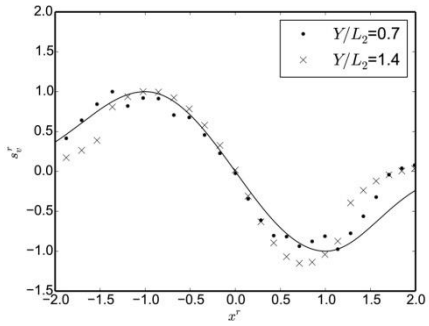

(c) $A = 2$

Fig. 12 Variations of the reduced lateral perturbation parameter with the reduced x coordinates. The variations are calculated based on CFD simulations results of the hill models with the aspect ratios of $1/2$, 1 and 2

Fig. 12 also contains the variations of $s_v{}^r$ with x^r calculated using the CFD simulation results corresponding to the hill aspect ratios of $1/2$ and 2. It is clear that the scattered points agree, in general, with the theoretical curve in the region where $x^r < 0$.

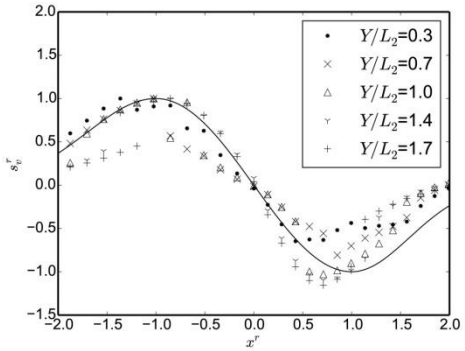

(a) H = 150 m

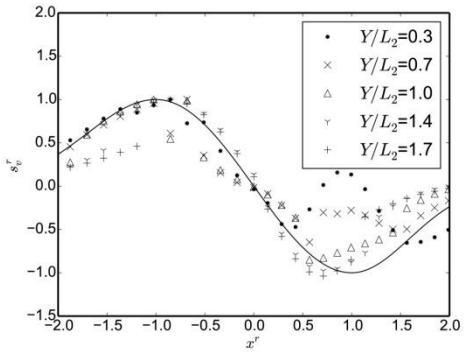

(b) H = 200 m

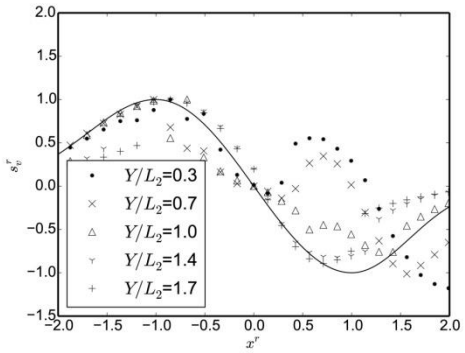

(c) H = 250 m

Fig. 13 Variations of reduced lateral perturbation parameter with the reduced x coordinates. The variations are calculated based on the CFD simulation results of the hill models with the hill heights of 150 m, 200 m and 250 m

When comparing Figs. 12(a) and 12(c) to Fig. 12(b), it is found that the agreement between the scattered points and the theoretical curve is slightly worse in the region $x^r < 0$ for the case where the aspect ratio of the hill equals $1/2$., The deviation of the scattered points from the theoretical curve is also observed for the case where the hill aspect ratio equals $1/3$. As a result, it can be asserted that Eq. (6) is less accurate, for calculating the horizontal variations of model parameters in the windward zone of the hill, when the hill aspect ratio less than 1. In fact, the lateral perturbation parameter in the wake zone is no longer only a function of x^r when the hill aspect ratio is less than 1.

As in Fig. 12, Fig. 13 presents the variations of ${s_v}^r$ with x^r calculated based on the CFD simulation results corresponding to hill heights of 150 m, 200 m, 250 m. Different from the comparison shown in Fig, 12, Fig. 13 indicates that the hill height, and hence the overall hill slope, has little impact on how close the scattered points calculated based on the CFD simulation results are to the theoretical curve, especially in the windward zone ($x^r < 0$). Hence, it can be concluded that Eq. (6) always provides good estimations of the lateral perturbation parameter in the windward zone regardless of the hill height. Since the scattered points deviate from the pattern expressed by the theoretical curve in a region immediately behind the hill ($y/L_2 < 0.5$ and $x^r > 0$) when the hill height exceeds 200 m, it is postulated that the influence of the hill height, and hence the hill slope, on the direction changes mainly restricts into the area immediately behind the hill.

Since the calculation of the lateral perturbation parameter involves the local hill slope, it is reasonable to speculate that the hill local slope has appreciable impact on the applicability of Eq. (6). As a result, it is necessary to use a hill whose shape is not described by Eq. (7) to evaluate the impact of general hill shape on the validity of the proposed model. Specifically, hills whose surface elevation calculated as

$$z = H - \frac{H}{2L_1}\sqrt{x^2 + Ay^2} \tag{16}$$

were employed to set up the model for additional CFD simulations. In Eq. (16), all symbols have the same meaning as in Eq. (7). In order to be comprehensive, the aspect ratios of the hills employed in the additional simulation are 1,2 and 3 while the hill height is kept constant at 100 m. Unlike the hill whose shape is described by Eq. (2), the hills employed in the additional CFD simulation have a constant local slope.

Fig. 14 presents the variation of ${s_v}^r$ with x^r, calculated based on the results from the additional CFD simulation, as in Figs. 12 and 13. I t has been found from examining the variation of ${s_v}^r$ shown in Fig. 14 that Eq. (6) is not universally applicable. Especially in the regions where $x^r < -1$ and $x^r > 1$, the scattered point calculated based on the CFD simulation results deviates from the theoretical curve considerably. More importantly, in the regions where $x^r < -1$ and $x^r > 1$, the clear pattern shown by the scattered points in the region where $-1 < x^r < 1$ is absent. Such a feature implies that the lateral perturbation parameter in this case is no longer a function of only x^r (the lateral variation of ${s_v}^r$ is no longer negligible). In the region where the scattered point close to the theoretical curve, it has been found that the local slope calculating according to Eq. (16), in both the longitudinal and lateral directions, is close to the local slope calculated according to Eq. (7). Therefore, it is hypothesized that Eq. (6) is only valid for the hill whose local slope varies gradually. Alternatively, Eq. (6) is able to describe the horizontal variation of the direction changes, when the hill local slope gradually varies from 0 (at the hill foot) to the maximum value (at the mid-slope point), and then back to 0 (at the hill top).

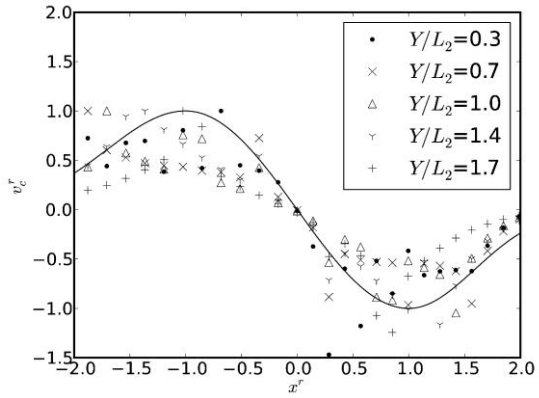

(a) $A = 1$

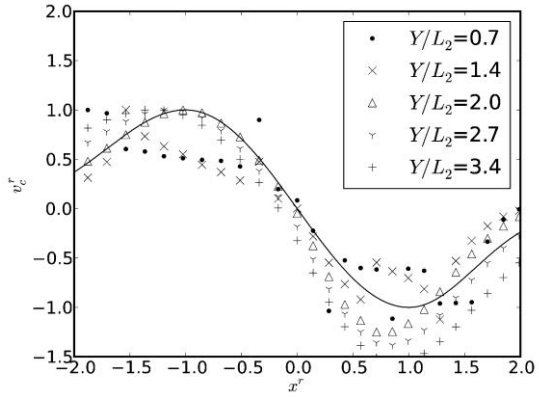

(b) $A = 2$

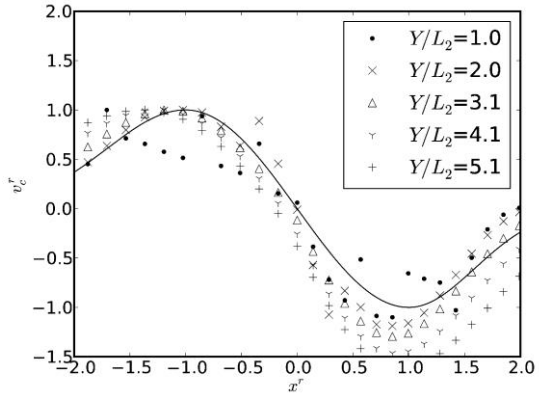

(c) $A = 3$

Fig. 14 Variations of reduced lateral perturbation parameter with the reduced x coordinates. The variations are calculated based on the CFD simulation results of the constant-local-slope hill models with the aspect ratios of 1, 2 and 3

4. Conclusions

In a wind field perturbed by hilly topography, it is obvious that both wind speeds and direction are influenced by the underlying terrain. While the influence on wind speeds (the speed-up effect) has been thoroughly studied, the influence on the wind directions has seldom been a topic for previous researches. Consequently, there are sophisticated models available to describe the speed-up effect induced by hilly topographies, but there are few models available to describe the direction changes. In the companion paper (Weerasuriyaa *et al*. 2016), an engineering model has been proposed based on the results from a series of wind-tunnel model experiments. Although, on a preliminary assessment, the wind-tunnel test results have validated the proposed model, it is necessary to further investigate its applicability and limitations. Consequently, CFD techniques were employed to simulate the wind field perturbed by hills with different geometries.

As the model describes the direction changes in the vertical direction and in the horizontal plane separately, the applicability of Eqs. (2) and (6) were evaluated individually. For the vertical variation, it has been found that Eq. (2) acceptably approximates the vertical variations of u and v in a wind field perturbed by a low hill. When the hill aspect ratio deviates considerably from 1, the estimates made according to Eq. (2) are, in general, less accurate. As expected, the applicability of Eq. (2) reduces with the increasing hill height. It is suggested that Eq. (2) in the case where the overall hill slope exceeds $20°$ should be used with caution. For the validity of Eq. (6), it has been found that the theoretical curves calculated by Eq. (6) are slightly different from the CFD simulation results in the windward zone when the hill aspect ratio is less than 1. In the wake zone, it can be concluded that Eq. (6) is not applicable when the hill aspect ratio is less than 1. When the hill height varies from 100 m to 300 m, which corresponds to the variation of the overall hill slope from $9.68°$ to $27.10°$, the agreement between the CFD simulation results and the theoretical curves remains unchanged in the windward zone. Based on CFD simulation results, it has been found that Eq. (6) is only valid in the case where the hill local slope varies gradually from 0 (at the hill foot) to the maximum value (at the mid-slope point) and then back to 0 (at the hill top).

Acknowledgements

The work described in the present paper is supported by the Economy, Trade and Information Commission of Shenzhen Municipality (Project No. 201510150880 and SZHY2014-B01-001).

References

Balogh, M., Parente, A. and Benocci, C. (2012), "RANS simulation of ABL flow over complex terrains applying an Enhanced k-e model and wall function formulation: Implementation and comparison for fluent and OpenFOAM", *J. Wind Eng. Ind. Aerod*., **104-106**, 360-368.

Bitsuamlak, G.T., Stathopoulos, T. and Bedard, C. (2004), "Numerical evaluation of wind flow over complex terrain: Review", *J. Aerospace Eng*., **17**(4), 135-145.

Bitsuamlak, G., Stathopoulos, T. and Bedard, C. (2006), "Effects of upstream two-dimensional hills on design wind loads: a computational approach", *Wind Struct.*, **9**(1), 37-58.

Derickson, R. and Peterka, J.A. (2004), "Development of a powerful hybrid tool for evaluating wind power in complex terrain: Atmospheric numerical models and wind tunnels", *Proceedings of the 23rd ASME Wind Energy Symposium*, Reno, Nevada.

Engineering Science Data Unit (1993), *Mean wind speeds over hills and other topography, Section No. 91043*, London: IHS ESDU.

Hitchcock, P.A., Kwok, K.C.S., Wong, K.S. and Shum, K.M. (2010), "The effects of topography on local wind-induced pressures of a medium-rise building", *Wind Struct.*, **13**(5), 433-449.

Jackson, P.S. and Hunt, J.C.R. (1975), "Turbulent wind flow over a low hill", *Q. J. Roy. Meteorol. Soc.*, **101**(430), 929-955.

Jazcilevich, A.D., García, A.R. and Caetano, E. (2005), "Locally induced surface air confluence by complex terrain and its effects on air pollution in the valley of Mexico", *Atmos. Environ.*, **39**(30), 5481-5489.

Kim, H.G., Patel, V.C. and Lee, M.C. (2000), "Numerical simulation of wind flow over hilly terrain", *J. Wind Eng. Ind. Aerod.*, **87**(1), 45-60.

Lindley, D., Neal, D., Pearse, J. and Stevenson, D. (1981), "The effect of terrain and construction method on the flow over complex terrain models in a simulated atmospheric boundary layer", *Proceedings of the 3rd British Wind Energy Association Wind Energy Conference*, Cranfield, UK.

Liu, B., Qu, J., Zhang, W. and Qian, G. (2011), "Numerical simulation of wind flow over transverse and pyramid dunes", *J. Wind Eng. Ind. Aerod*., **99**(8), 879-888.

Lubitz, W.D. and White, B.R. (2007), "Wind-tunnel and field investigation of the effect of local wind direction on speed-up over hills", *J. Wind Eng. Ind. Aerod.*, **95**(8), 639-661.

Mason, P.J. and Sykes, R.I. (1979), "Flow over an isolated hill of moderate slope", *Q. J. Roy. Meteorol. Soc.*, **105**(444), 383-395.

Miller, C.A. and Davenport, A.G. (1998), "Guidelines for the calculation of wind speed-ups in complex terrain", *J. Wind Eng. Ind. Aerod.*, **74-76**, 189-197.

Palma, J., Castro, F., Ribeiro, L., Rodrigues, H. and Pinto, A. (2008), "Linear and nonlinear models in wind resource assessment and wind turbine micro-siting in complex terrain", *J. Wind Eng. Ind. Aerod.*, **96**(12), 2308-2326.

Snyder, W. (1973), "Similarity criteria for the application of fluid models to the study of air pollution meteorology", *Bound. – Lay. Metrol.*, **3**(1), 113-134.

Sumner, J., Watters, C.S. and Masson, C. (2010), "CFD in wind energy: the virtual, multiscale wind tunnel", *Energies*, **3**(5), 989-1013.

Taylor, P.A., Walmsley, J.L. and Salmon, J.R. (1983), "A simple model of neutrally stratified boundary-layer flow over real terrain incorporating wavenumber-dependent scaling", *Bound. – Lay. Metrol*., **26**(2), 169-189.

Tominaga, Y., Mochida, A., Yoshie, R., Kataoka, H., Nozu, T., Yoshikawa, M. and Shirasawa, T. (2008). "AIJ guidelines for practical applications of CFD to pedestrian wind environment around buildings", *J. Wind Eng. Ind. Aerod.*, **96**(10-11), 1749-1761.

Uchida, T. and Ohya, Y. (2003), "Large-eddy simulation of turbulent airflow over complex terrain", *J. Wind Eng. Ind. Aerod.*, **92**(1-2), 219-229.

Weerasuriyaa, A.U., Hu, Z.Z., Li, S.W. and Tse, K.T. (2016), "Wind direction field under the influence of topography, Part I: A descriptive model", *Wind Struct*., Accepted.

Yang, Y., Gu, M., Chen, S. and Jin, X. (2009), "New inflow boundary conditions for modelling the neutral equilibrium atmospheric boundary layer in computational wind engineering", *J. Wind Eng. Ind. Aerod*,, **97**(2), 88-95.

JH